Parallel-beam ROI reconstruction with differentiated backprojection and angularly subsampled complementary sinograms

Aymeric Reshef, Tina Nikoukhah, Cyril Riddell, Yves Trousset, Saïd Ladjal, and Isabelle Bloch

***Abstract*—Recently, we introduced a parallel-beam two-pass analytical reconstruction that allows truncation to be accounted for in the image domain rather than the projection domain. In particular, we showed that backprojection of a vastly angularly undersampled sinogram of un-truncated data could be used to extrapolate the backprojection of a finely sampled, fully truncated sinogram of the same object to perform more accurate region-of-interest (ROI) imaging. The same extrapolation idea can be performed using differentiated backprojection (DBP). The goal of this study is to give a general DBP-based formula when reconstructing a finite set of projections in parallel geometry. We discuss the discretization of this formula, in particular when the image grid size is large with respect to the number of projections, and we show how it can be applied to our extrapolation problem.**

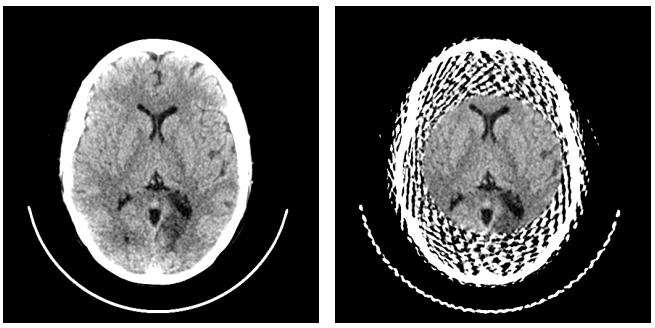

(a) Reference image (b) With 45 un-truncated projections

Fig. 1: Dual-rotation reconstruction with a two-pass Hilbert-transformed DBP (DBP-HT-2) [3]. Window width: 50 HU.

I. Introduction

We address the classic case of interior tomography, when truncation due to the limited size of the detector defines a centered region-of-interest (ROI) of an object for which no complete projection is available. Without additional a priori knowledge, exact reconstruction of this ROI is not possible from the truncated data. Even though the amount of required a priori data may be considered tiny [1], it is still usually unavailable. A second approach is to complement the truncated data with a second acquisition. In the context of very high-resolution imaging, only the ROI is scanned at very high resolution, because the cost of scanning the entire object is prohibitive either in terms of scanning time, dose, or both. A second acquisition encompassing the full object at standard resolution removes the truncation artifacts through extrapolation of the truncated high-resolution data with the lower-resolution complete data. In the context of C-arm CBCT, we proposed a dual-rotation scheme, where a complementary acquisition of un-truncated data at same resolution but angularly vastly undersampled removes truncation artifacts using a standard least-square iterative reconstruction [2]. The iterative approach makes full use of the two sets of data without any explicit data extrapolation. For an analytical alternative, the extrapolation must be explicit and we showed that it is most conveniently achieved in the image space after backprojection of both data sets [3] (Fig. 1). Here, we look at the specific case of extrapolating the differentiated backprojection (DBP) within the context of a general DBP-based reconstruction formula for parallel-beam geometry.

The general DBP formula is presented in Section II, along with the DBP-based extrapolation for ROI imaging. The specific case of using standard DBP images is studied in Section III. Simulations on forward projections of a clinical head CT slice are described in Section IV. The results are shown in Section V.

A. Reshef (corresponding author: aymeric.reshef@ge.com) is with GE Healthcare, Buc, France, and LTCI, Télécom ParisTech, Université Paris-Saclay, Paris, France. T. Nikoukhah, C. Riddell and Y. Trousset are with GE Healthcare, Buc, France. S. Ladjal and I. Bloch are with LTCI, Télécom ParisTech, Université Paris-Saclay, France. This work was supported by the CIFRE grant No. 873/2014 from the French Association Nationale de la Recherche et de la Technologie (ANRT).

II. General DBP reconstruction formula

A. Notations

We parametrize the orientation of a parallel beam by its direction $\boldsymbol{\theta} = (\cos\theta, \sin\theta)^T$, where $\theta \in [0, \pi]$. The detector is orthogonal to the beam and oriented along $\boldsymbol{\theta}^\perp = (-\sin\theta, \cos\theta)^T$. Any point $\boldsymbol{x}$ is thus related to its detector coordinate $u_\theta(\boldsymbol{x})$ by equation $u_\theta(\boldsymbol{x}) = \boldsymbol{x} \cdot \boldsymbol{\theta}^\perp$. The Hilbert transform of a 1D signal is denoted $\mathcal{H}$, and we denote $\mathcal{H}_\alpha$, the 2D filter that applies $\mathcal{H}$ over all the lines colinear to $\boldsymbol{\alpha}^\perp$. We denote p_θ, the projection available at angle θ, and p'_θ the differentiation of p_θ along $\boldsymbol{\theta}^\perp$. We denote $\mathcal{B}_\theta$ the backprojection operator from angle θ, defined as: $\mathcal{B}_\theta[q](\boldsymbol{x}) = q(u_\theta(\boldsymbol{x}))$ for any projection q. For a set of angular positions Θ, we define p'_Θ as the collection $\{p'_\theta\}_{\theta\in\Theta}$. We further write $\sigma^\alpha_\Theta \otimes p'_\Theta = \{\mathrm{sgn}(\boldsymbol{\alpha}\cdot\boldsymbol{\theta})\cdot p'_\theta\}_{\theta\in\Theta}$, and $\mathcal{B}_\Theta[p'_\Theta] = \int_\Theta \mathcal{B}_\theta[p'_\theta]\,\mathrm{d}\theta$.

We consider a finite set of projections over interval $[0, \pi]$. The interval is split into N angular sectors of aperture $\Delta\theta = \frac{\pi}{N}$. We denote $\Theta = \left\{\theta_n = \left(n - \frac{1}{2}\right)\Delta\theta, n = 1, \cdots, N\right\}$ the set of acquired angular positions.

B. Splitted DBP formula

Given a partition $\{\Theta_k\}_{k=1,\cdots,K}$ of Θ, one can reconstruct image f through:

$$\begin{aligned} f &= \frac{1}{2\pi}\sum_{k=1}^{K}\mathcal{H}_{\alpha_k}\mathcal{B}_{\Theta_k}\left[\sigma_{\Theta_k}^{\alpha_k}\otimes p'_{\Theta_k}\right] \\ &= \frac{1}{2\pi}\sum_{n=1}^{N}\mathcal{B}_{\theta_n}\mathcal{H}\left[p_{\theta_n}\right], \end{aligned} \tag{1}$$

where $\alpha_k \in [0,\pi]$ is such that $\boldsymbol{\alpha}_k \cdot \boldsymbol{\theta} = \cos(\theta-\alpha_k) \neq 0$ for all $\theta \in \Theta_k$. The most right handside is the standard filtered backprojection (FBP) and the result holds because one can replace Hilbert transform $\mathcal{H}$ prior to backprojection by $\mathcal{H}_{\alpha_k}$ after backprojection (see Appendix). If all partition sets Θ_k are singletons ($K=N$), we have one filtering direction per projection, typically $\boldsymbol{\theta}_k^{\perp}$, as in standard FBP. On the other hand, if $K=1$, the only admissible filtering direction is given by $\alpha_1 = \frac{\pi}{2}$, resulting in a filtering step along the x-axis, as in the single-pass Hilbert-transformed DBP (DBP-HT-1) algorithm [4].

For $K=2$, we divide Θ into frontal views and lateral views. Frontal views correspond to $\Theta_{\mathrm{FRT}} = \Theta \cap \left[\frac{\pi}{4},\frac{3\pi}{4}\right]$. We select $\alpha_{\mathrm{FRT}} = \frac{\pi}{2}$, yielding a horizontal filtering along the y-axis. Lateral views correspond to $\Theta_{\mathrm{LAT}} = \Theta \setminus \Theta_{\mathrm{FRT}}$. We select $\alpha_{\mathrm{LAT}} = 0$, yielding a vertical filtering along the y-axis. We call this reconstruction method the two-pass Hilbert-transformed DBP (DBP-HT-2). This common formula proves that DBT-HT-2, DBP-HT-1, and FBP, applied to a finite set of projections, yield the same reconstruction.

C. DBP extrapolation for ROI imaging

When considering two acquisitions from the same detector with different angular sampling but equal detector resolution, the complete data cannot be used to directly extrapolate the truncated ones because such data are not available for all angles. Alternatively, the DBP of each sinogram correspond to two images: one that is uniformly sampled but at a low rate, and one that is finely sampled but not uniformly over the image space due to truncation of the projections. In Fig. 2, we illustrate the merge of both DBP images. The central field of view (FOV) corresponds to the ROI (area inside the orange circle); it is made of the finely sampled DBP where the sampling is also uniform. Outside the ROI, the coarsely sampled DBP is used instead because it is uniformly sampled. At the edges of the ROI, a smooth transition is ensured using the radial weighting function:

$$\eta(r) = \frac{1}{2}\left(1-\cos\left(\pi\cdot\frac{r-r_\Omega}{\Delta r}\right)\right), \tag{2}$$

where r_Ω denotes the radius of the ROI, and Δr is the transition zone radial width. The DBP extrapolation actually consists of K extrapolations, one per partition subset. Fig. 2a illustrates such extrapolation for the frontal views of DBP-HT-2. Hilbert-filtering for all rows crossing the ROI will not be truncated in this case, since these rows have a finite support. In contrast, when using $K=1$ and DBP-HT-1 (Fig. 2b), all Hilbert lines are truncated.

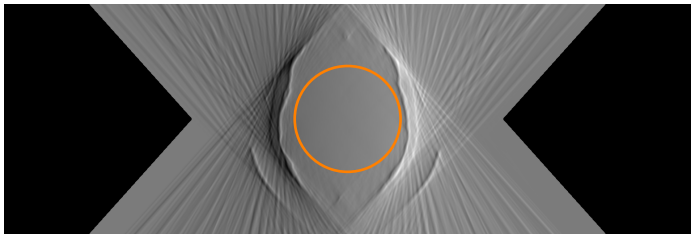

(a) DBP-HT-2, $\Theta_2 = \left[\frac{\pi}{4},\frac{3\pi}{4}\right]$

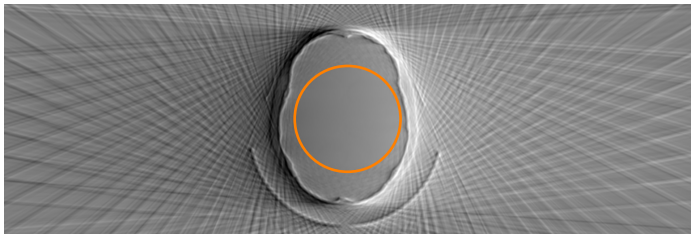

(b) DBP-HT-1, $\Theta_1 = [0,\pi]$

Fig. 2: Dual-rotation DBP extrapolation for ROI imaging. (a) The Hilbert transform can be computed for all horizontal lines crossing the circular ROI (orange circle). (b) The Hilbert transform is truncated for all horizontal lines crossing the ROI.

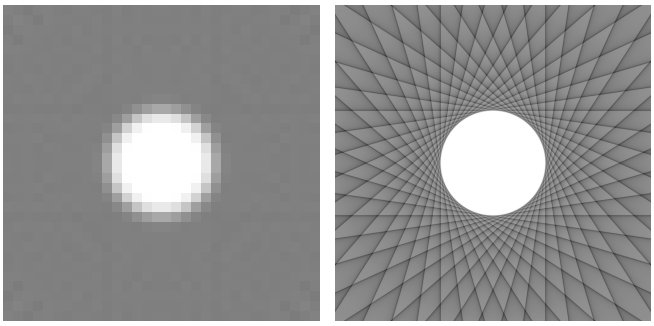

(a) $N=22$, $M=32$ (b) $N=22$, $M=1024$

Fig. 3: Angular sampling, resolution and image support.

III. ROI IMAGING WITH DBP-HT-1

A. Discretization

Reconstruction from a finite set of projections means estimating the image from a finite set of angular samples in the Fourier space according to the central-slice theorem. Because the images have a finite support, the finite Fourier sampling leads to sampling artifacts, which depends on the defined sampling of the images themselves, typically two-dimensional grids of size $M \times M$. This point is illustrated in Fig. 3 where the image is reconstructed from a set of $N=22$ projections using Eq. (1) with $K=N$ over two different grids ($M=32$ and $M=1024$).

When comparing both images, we note the classical streak artifacts on the right high-resolution image that are not visible on the left. A second consideration needs to be mentioned: the sampling artifacts cover the whole grid beyond the object and are actually truncated by the finite size of the image grid. In reality, the issue is the same on both images, but with a different intensity.

B. Undersampling

The general formula in Eq. (1) does not lead to equivalent results for any image f because the computation of the Hilbert transform is sensitive to truncation. When using $K > 1$, it is always possible to define filtering directions $\boldsymbol{\alpha}_k^{\perp}$ such that the Hilbert transform $\mathcal{H}_{\alpha_k}$ is applied to non-truncated signals if the original projections are not truncated. For the case $K = 1$, this is not true anymore, but if one assumes that the result of the Hilbert transform has a finite support, then the truncated Hilbert transform can be applied [4]. Since, as already mentioned, the reconstruction of an image from a finite set of projections has an infinite support, DBP-HT-1 cannot be computed. In practice, there exists a large enough number of projections such that the sampling artifacts can be neglected and the support considered finite. In the case of significant under-sampling ($N \ll M$), the sampling artifacts are significant over the whole reconstruction grid and beyond. However, one solution lies in Fig. 3 itself: there exists a coarser reconstruction grid of sampling $M' \approx N$, or equivalently, there exists a low-pass version of the DBP that can be used to reconstruct a low-pass version of f.

IV. Simulations

A diagnostic CT slice of a brain (Fig. 1a) was forward-projected to simulate 720 noise-free parallel-beam projections of 576 bins, sampling uniformly $[0, \pi]$. Truncated data p_{T} consist of the 720 projections with a centered digital truncation corresponding to a centered, circular 2D region-of-interest Ω of diameter 256 pixels. Full-FOV projections $p_{\mathrm{F},s}$ consist of N_{F} samples of the 720 original projections, again uniformly distributed over $[0, \pi]$. We write $N_{\mathrm{F}} = 720/s$, where s is the down-sampling factor; we used $s = 2^q$ with q integer varying from 0 ($s = 1$) to 7 ($s = 128$). The images are sampled on a 512×512 square grid. In order to use DBP-HT-1, the DBP of each sinogram is computed, that of $p_{\mathrm{F},s}$ being further filtered by 2D Gaussian filtering parameterized by its standard deviation σ, that is varied from 0 (no smoothing) to 40 pixels by steps of 5 pixels. The DBP are merged using the weighting function of Eq. (2) with $\Delta r = 15$ pixels. All Hilbert transforms are computed as proposed in [5]. The image quality was assessed by the mean relative error (MRE) between each reconstructed image $f_{\sigma,s}$ with respect to the reference image $f_{\mathrm{ref}} = f_{0,1}$, computed over Ω, as:

$$\mathrm{MRE}_{\sigma,s} = \frac{1}{\mathrm{Card}(\Omega)} \sum_{\boldsymbol{x} \in \Omega} \frac{|f_{\sigma,s}(\boldsymbol{x}) - f_{\mathrm{ref}}(\boldsymbol{x})|}{|f_{\mathrm{ref}}(\boldsymbol{x})|}. \qquad (3)$$

V. Results

The mean relative errors are shown in Fig. 4. For each value of s, the optimal smoothing parameter σ^* achieving the minimum MRE is indicated with a green dot. These values are also recalled in Table I. Although for $N_{\mathrm{F}} \geq 90$ ($s \leq 16$) the minimum MRE values seem to follow a smooth curve on the plane (σ, s), they are significantly higher and towards much higher σ values when N_{F} drops to as few as 22 ($s \geq 32$). This shows that filtering is not sufficient when s is too high.

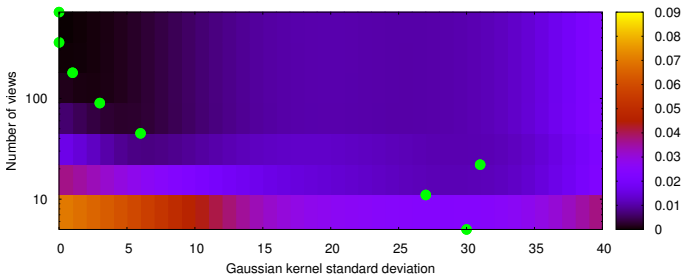

Fig. 4: MRE inside the ROI as a function of angular sampling and of the Gaussian smoothing filter.

s	N_{F}	σ^*	$\mathrm{MRE}_{\sigma^*,s}$ (%)
1	720	0	0.00
2	360	0	$8 \cdot 10^{-3}$
4	180	1	0.04
8	90	3	0.10
16	45	6	0.30
32	22	31	1.10
64	11	27	1.11
128	5	30	3.72

Table I: Optimal smoothing parameter σ and corresponding MRE for each angular subsampling ratio s.

Reconstructed images with the optimal values σ^* according to the MRE criterion are shown in Fig. 5, that compares reconstruction $f_{0,s}$, that is, without Gaussian smoothing, to $f_{\sigma^*,s}$. For all values of $s > 2$, the absence of Gaussian smoothing resulted in reconstructed ROI suffering from horizontal streaks due to the invalid inversion of the Hilbert transform, even with 90 full-FOV projections. For $s < 32$, the optimal smoothing strongly reduced the impact of horizontal streaks in the ROI, resulting in values of the MRE of 0.30% for $s = 16$ (Fig. 5e) and 0.10% for $s = 8$ (Fig. 5f). For $s = 32$ (Fig. 5d), the strong Gaussian smoothing is shown to reduce the effect of the horizontal streaks, but the reconstructed image suffers from residual low-frequency non-uniformities. For higher values of s this issue worsened (images not shown).

VI. Discussion

In this study, we introduced a general formula for DBP-based reconstruction in parallel-beam geometry and applied it to solve the interior problem with a few extra full-FOV projections. This led us to investigate the case of reconstructing vastly angularly subsampled acquisitions with DBP-HT-1. Our study shows that because the key requirement of a finite support is not met, this algorithm cannot be used "as is". An alternative two-pass method (DBP-HT-2) does not suffer from this issue. However, we showed that subsampling could be mitigated by Gaussian smoothing of the areas outside the ROI. This is important because DBP-HT-1 is the only algorithm covered by our formula that allows for DBP extrapolation when reconstructing a single line, whereas DBP-HT-2 is applicable to reconstructing the full ROI only.

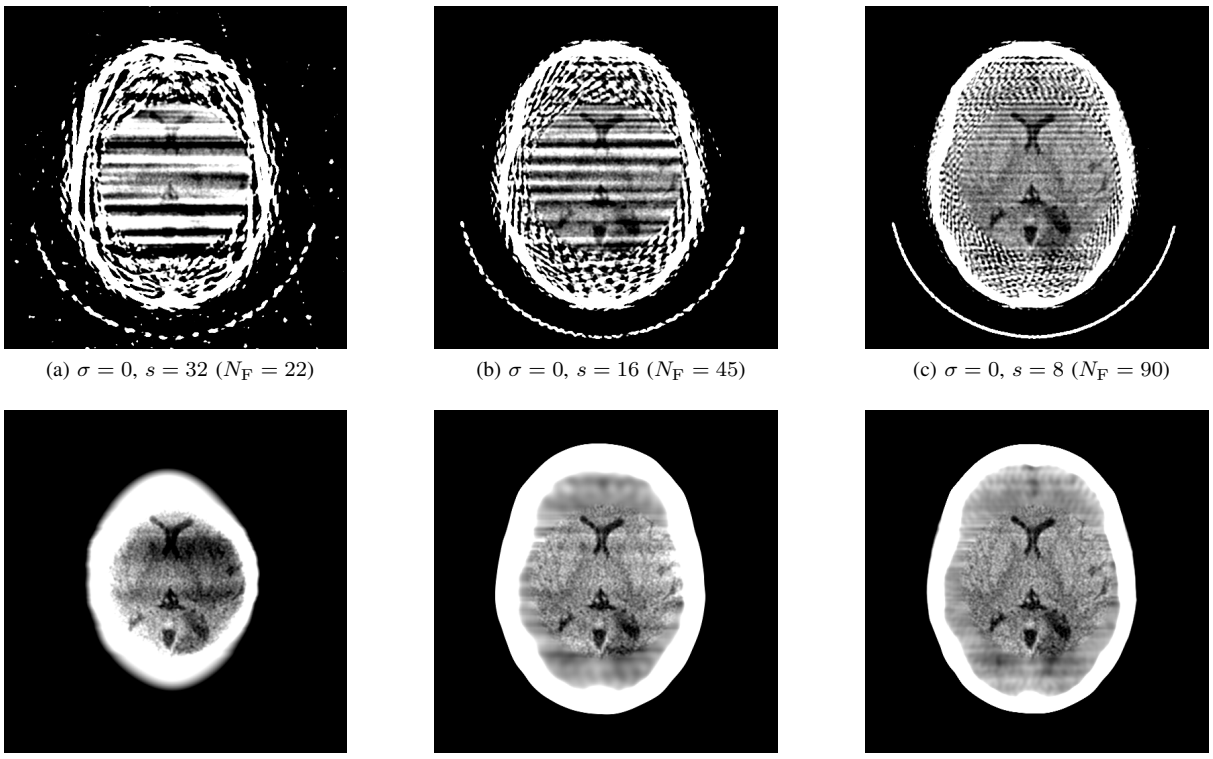

(a) $\sigma = 0$, $s = 32$ ($N_{\mathrm{F}} = 22$) (b) $\sigma = 0$, $s = 16$ ($N_{\mathrm{F}} = 45$) (c) $\sigma = 0$, $s = 8$ ($N_{\mathrm{F}} = 90$)

(d) $\sigma = 31$, $s = 32$ ($N_{\mathrm{F}} = 22$) (e) $\sigma = 6$, $s = 16$ ($N_{\mathrm{F}} = 45$) (f) $\sigma = 3$, $s = 8$ ($N_{\mathrm{F}} = 90$)

Fig. 5: Dual-rotation reconstruction with DBP extrapolation, $K = 1$, no smoothing (top) and optimal smoothing (bottom) of the full-FOV projections. Window width: 50 HU.

APPENDIX
PROOF OF EQ. (1)

Let $\theta \in [0, \pi]$ and $b_\theta = \mathcal{B}_\theta \left[p'_\theta\right]$. Let $\boldsymbol{x} \in \mathbb{R}^2$, and $\alpha \in [0, \pi]$ such that $\boldsymbol{\theta} \cdot \boldsymbol{\alpha} \neq 0$. We write:

$$b_\theta(\boldsymbol{x}) = p'_\theta(\boldsymbol{x} \cdot \boldsymbol{\theta}^\perp) = p'_\theta\left(A(\boldsymbol{x} \cdot \boldsymbol{\alpha}^\perp) + B\right), \tag{4}$$

where $A = \boldsymbol{\theta} \cdot \boldsymbol{\alpha} \neq 0$ and $B = (-\boldsymbol{x} \cdot \boldsymbol{\alpha})\boldsymbol{\theta} \cdot \boldsymbol{\alpha}^\perp$. The Fourier transform of $\mathcal{A}_{A,B}[p'_\theta] : u \mapsto p'_\theta(Au + B)$ is related to the Fourier transform of p'_θ through:

$$\mathcal{F}\left[\mathcal{A}_{A,B}[p'_\theta]\right](\rho) = \frac{1}{|A|}\mathcal{F}\left[p'_\theta\right]\left(\frac{\rho}{A}\right)e^{2i\pi\frac{\rho}{A}B}. \tag{5}$$

Hence, applying $\mathcal{H}_\alpha$ to b_θ is equivalent to multiplying the right-hand side of Eq. (5) by $-i\,\mathrm{sgn}(\rho) = -i\,\mathrm{sgn}(A)\,\mathrm{sgn}\left(\frac{\rho}{A}\right)$, prior to taking the inverse Fourier transform:

$$\mathcal{H}_\alpha\left[b_\theta\right](\boldsymbol{x}) = \frac{1}{A}\int_{-\infty}^{+\infty} -i\,\mathrm{sgn}\left(\frac{\rho}{A}\right)\mathcal{F}\left[p'_\theta\right]\left(\frac{\rho}{A}\right)e^{2i\pi\frac{\rho}{A}(A\boldsymbol{x}\cdot\boldsymbol{\alpha}^\perp+B)}\mathrm{d}\rho. \tag{6}$$

Taking the change of variables $\rho' = \frac{\rho}{A}$ yields:

$$\mathcal{H}_\alpha\left[b_\theta\right](\boldsymbol{x}) = \mathrm{sgn}(A)\int_{-\infty}^{+\infty} -i\,\mathrm{sgn}\left(\rho'\right)\mathcal{F}\left[p'_\theta\right]\left(\rho'\right)e^{2i\pi\rho'(A\boldsymbol{x}\cdot\boldsymbol{\alpha}^\perp+B)}\mathrm{d}\rho'. \tag{7}$$

The right-hand side of Eq. (7) is equal to $\mathrm{sgn}(A)\mathcal{B}_\theta\mathcal{H}\left[p'_\theta\right]$. In other words:

$$\mathcal{H}_\alpha\mathcal{B}_\theta\left[\mathrm{sgn}(\boldsymbol{\theta}\cdot\boldsymbol{\alpha})\cdot p'_\theta\right] = \mathcal{B}_\theta\mathcal{H}\left[p'_\theta\right]. \tag{8}$$

If $\Theta_k = \{\theta_{k,1}, \cdots, \theta_{k,\mathrm{Card}(\Theta_k)}\}$ is a partition subset of Θ, where $\theta_{k,1} < \cdots < \theta_{k,\mathrm{Card}(\Theta_k)}$, we can choose a common admissible angle α such that $\boldsymbol{\alpha}\cdot\boldsymbol{\theta} \neq 0$ and Eq. (8) holds for all $\theta \in \Theta_k$. We denote α_k this common value, so that:

$$\mathcal{H}_{\alpha_k}\mathcal{B}_{\Theta_k}\left[\sigma_{\Theta_k}^{\alpha_k} \otimes p'_{\Theta_k}\right] = \sum_{\theta\in\Theta_k}\mathcal{B}_\theta\mathcal{H}\left[p'_\theta\right]. \tag{9}$$

Summing the contributions of all the partition subsets yields:

$$\sum_{k=1}^{K}\mathcal{H}_{\alpha_k}\mathcal{B}_{\Theta_k}\left[\sigma_{\Theta_k}^{\alpha_k} \otimes p'_{\Theta_k}\right] = \sum_{\theta\in\Theta}\mathcal{B}_\theta\mathcal{H}\left[p'_\theta\right], \tag{10}$$

which concludes the proof.

REFERENCES

[1] H. Kudo, M. Courdurier, F. Noo, and M. Defrise, "Tiny a priori knowledge solves the interior problem in computed tomography," *Physics in Medicine and Biology*, vol. 53, no. 9, p. 2207, 2008.

[2] A. Reshef, C. Riddell, Y. Trousset, S. Ladjal, and I. Bloch, "Dual-rotation C-arm cone-beam computed tomography to increase low-contrast detection," *Medical Physics*, vol. 44, no. 9, pp. e164–e173, 2017.

[3] ——, "Divergent-beam backprojection-filtration formula with applications to region-of-interest imaging," in *Proceedings of the 5th CT Meeting*, Salt Lake City, USA, May 2018.

[4] F. Noo, R. Clackdoyle, and J. D. Pack, "A two-step Hilbert transform method for 2D image reconstruction," *Physics in Medicine and Biology*, vol. 49, no. 17, p. 3903, 2004.

[5] J. You and G. L. Zeng, "Explicit finite inverse Hilbert transforms," *Inverse Problems*, vol. 22, no. 3, p. L7, 2006.